

Propagation of a partially coherent focused X-ray beam within a planar X-ray waveguide

J. H. H. Bongaerts,^a C. David,^b M. Drakopoulos,^c
M. J. Zwanenburg,^a G. H. Wegdam,^a T. Lackner,^b
H. Keymeulen^b and J. F. van der Veen^{b*}

^aVan der Waals–Zeeman Institute, Valckenierstraat 65, 1018 XE Amsterdam, The Netherlands, ^bPaul Scherrer Institut, CH-5232 Villigen PSI, Switzerland, and ^cEuropean Synchrotron Radiation Facility, Grenoble, France. E-mail: friso.vanderveen@psi.ch

A linear-transmission Fresnel-zone-plate lens is used for coupling a monochromatic X-ray beam of 13.2 keV into a planar X-ray waveguide. The zone plate focuses the beam parallel to the entrance of the waveguide, by which means a flux enhancement of a factor of 54 inside the waveguide is obtained. This substantially enlarges the range of X-ray diffraction experiments that can be performed on samples confined within the waveguide. The coherent properties of the beam, as obtained at a third-generation synchrotron facility, are investigated by comparing the experimental data with numerical calculations in which partial coherence is taken into account by propagation of the mutual intensity function. The conditions for which the X-rays travelling through the waveguide are coherent are discussed.

Keywords: planar waveguide; X-rays; partial coherence; focusing; zone-plate lens; flux enhancement.

1. Introduction

The development of X-ray waveguides (Spiller & Segmueller, 1974; Feng *et al.*, 1993; Lagomarsino *et al.*, 1996; Zwanenburg *et al.*, 1999; Pfeiffer *et al.*, 2002) has made it possible to create narrow, intense and well defined X-ray beams. Such narrow beams allow for new types of X-ray scattering experiments on synchrotron facilities. One example is phase-contrast hard-X-ray microscopy on small objects that are placed behind the waveguide (Jark *et al.*, 1996; Lagomarsino *et al.*, 1997; Di Fonzo *et al.*, 2000). Another example is X-ray diffraction studies of fluids and solids in confined geometries (Zwanenburg, Bongaerts *et al.*, 2000). Previously, we have developed a tunable planar X-ray waveguide with an air gap to perform the latter type of experiments. In the waveguide setup, the sample under investigation is inserted into the air gap and thus constitutes the guiding layer of the waveguide (Zwanenburg *et al.*, 1999; Zwanenburg, Ficke *et al.*, 2000).

The tunable planar waveguide consists of two flat surfaces of a few millimeters in length that are positioned opposite to each other (see Fig. 1). The separation between the surfaces is typically between a few tens of nanometers and 1 μm . The X-ray beam is incident from the side under a glancing angle, and *via* a pre-reflection from the larger lower surface a standing-wave pattern is formed at the entrance of the waveguide. The electromagnetic (e.m.) waves are internally reflected by the inner interfaces and propagate inside the waveguide as so-called waveguide modes.

Since the width of an unfocused X-ray beam at a synchrotron facility is much larger (~ 0.5 mm in our case) than the waveguide gap W , most of the available flux is wasted if the waveguide modes are excited from the side. If the unexploited flux were to be made available to the waveguide, a wider range of diffraction studies on

samples with a low refractive-index contrast would be possible. Furthermore, the transverse coherence length along the vertical direction, $\xi_v \simeq 100$ μm , is much larger than the waveguide gap width W . By matching ξ_v to W , a large flux enhancement can be achieved without significantly affecting the degree of coherence of the e.m. waves inside the waveguide.

Here, we attain the flux enhancement by pre-focusing the incident beam onto the entrance of the waveguide with a one-dimensional diffractive lens (see Fig. 1). This creates a narrow line focus at the entrance of the waveguide. This approach is different from that in earlier experiments, where a resonant beam coupler (RBC) was employed to excite the waveguide modes (Lagomarsino *et al.*, 1996; Feng *et al.*, 1995; Pfeiffer *et al.*, 2000). In the RBC scheme, the flux enhancement is achieved by exciting the waveguide modes *via* an evanescent wave through a thin upper boundary layer. In this way a larger part of the incident beam is used. In our setup, however, the waveguide boundaries are thick slabs of silica, which will scatter and absorb the incident beam, rendering the RBC scheme ineffective. Furthermore, a disadvantage of the RBC is the fact that the modes that have been excited in the waveguide are constantly leaking out through the thin upper boundary layer.

In this paper, we present experiments in which a significant flux enhancement in the waveguide is achieved by pre-focusing of the X-ray beam. We examine the effects of the beam compression on the propagation of the waveguide modes through the waveguide. In §§2 and 3, the waveguide and the lens are discussed, respectively. The propagation of a partially coherent beam through the waveguide is described in §4 by way of the mutual intensity function. §5 discusses the experimental procedures and the results are shown in §6. A conclusion and brief outlook are given in §7.

2. The waveguide

The waveguide consists of two separate flat fused-silica disks (lower disk 25.4 mm, upper disk 5.5 mm) that are positioned opposite each other with piezo-driven motors (Fig. 1). An elaborate description of the waveguide setup is given by Zwanenburg, Ficke *et al.* (2000). The surfaces are coated with a 30 nm-thick aluminium layer with a

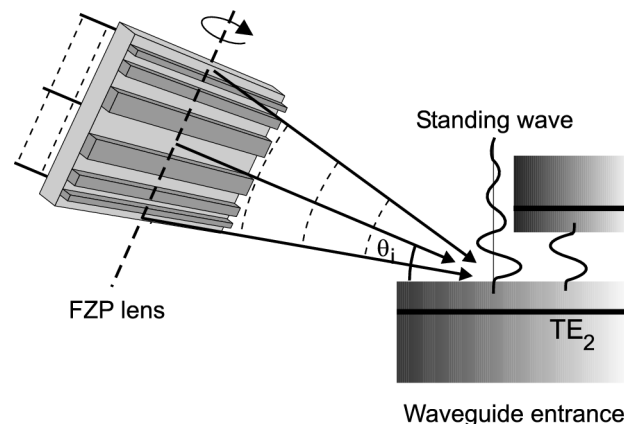


Figure 1

Schematic of the waveguide setup with the pre-focusing lens (not to scale). The guiding layer of the waveguide is the gap between the two closely spaced surfaces on the right. The dark layers in the substrates are the aluminium layers that form the optical interferometer for the FECO technique (see text). The incident beam is focused on the entrance of the waveguide by a transmission Fresnel-zone-plate lens, which can be removed. By rotating the lens around the axis indicated by the dashed line, the effective path length through the Fresnel zones can be adjusted to achieve optimal efficiency.

650 nm-thick silica spacer layer on top. The r.m.s. roughness of the top silica surface is below 1 nm. The two aluminium layers form an optical interferometer from which the surface separation and parallelism are monitored, making use of the technique of fringes of equal chromatic order (FECO) (Tolansky, 1970; Zwanenburg, Ficke *et al.*, 2000). The air gap between the opposing silica surfaces forms the X-ray guiding layer. The silica spacer layer enables us to position the surfaces at separations below optical wavelengths and still use the FECO technique (Bongaerts *et al.*, 2001).

If the angle of incidence θ_i is below the critical angle of total reflection, the incident beam is reflected by the larger lower surface. The reflected X-ray waves interfere with the non-reflected incident waves resulting in a sinusoidal standing-wave pattern at the entrance of the waveguide. The period of the standing-wave pattern decreases with increasing angle of incidence θ_i . When the gap width W is such that a node of the standing wave coincides with the upper surface, the standing wave corresponds in good approximation to a mode of the empty waveguide. Such a waveguide mode will propagate through the empty waveguide undisturbed.

The waveguide modes are solutions of the scalar wave equation

$$\left(\frac{\partial^2}{\partial x^2} + \frac{\partial^2}{\partial z^2}\right)E(x, z) + k^2 n^2(x, z)E(x, z) = 0, \quad (1)$$

where x is the coordinate in the confining direction (perpendicular to the waveguide surfaces) and z is the coordinate parallel to the propagation direction and parallel to the surfaces. The y coordinate is perpendicular to the propagation direction and parallel to the surfaces and is left out of the wave equation since the refractive index and the electric fields are considered to be independent of the y coordinate. Because the polarization of the X-rays in our experiments is parallel to the surfaces ($E_x = E_z = 0$), we only have propagation of transverse-electric (TE) modes. In (1), $k = 2\pi/\lambda$ is the wave number and $n(x, z)$ the position-dependent refractive index within the waveguide. For an empty waveguide, the refractive-index profile is independent of the z coordinate. In that case, we may separate the variables x and z and write the TE modes as $E_m(x, z) = \psi_m(x) \exp(-i\beta_m z)$, where β_m is the propagation constant, $\psi_m(x)$ is the mode profile of the transverse-electric mode TE_m and m is a non-negative integer mode number. For an empty waveguide, the normalized mode profiles $\psi_m(x)$ are to a good approximation given by (Zwanenburg *et al.*, 1999)

$$\psi_m(x) \simeq \begin{cases} (2/W)^{1/2} \sin(k\theta_m x) & x \in [0, W] \\ 0 & x \notin [0, W] \end{cases} \quad (2)$$

where $\theta_m = \lambda(m+1)/(2W)$ is the mode angle and the corresponding propagation constant is $\beta_m = k \cos(\theta_m)$. This approximation is valid if the penetration depth of the evanescent wave into the confining plates is much smaller than the gap width W .

The amplitude c_m of mode TE_m , excited at the entrance of the waveguide, is given by the overlap integral of the mode profile $\psi_m(x)$ with the incident e.m. field $E_{in}(x)$,

$$c_m = \int_{-\infty}^{+\infty} E_{in}(x) \psi_m(x) dx. \quad (3)$$

The e.m. field inside the waveguide is then given by

$$E(x, z) = \sum_{m=0}^{m_{\max}} c_m \psi_m(x) \exp(-i\beta_m z), \quad (4)$$

where m_{\max} is the maximum mode number. The summation is only over the guided modes and radiation modes have thus been neglected. A detailed description of the propagation of e.m. waves

inside a planar waveguide is given by Marcuse (1991) and Zwanenburg (2001).

3. Fresnel-zone-plate lens

The incident beam is focused onto the entrance of the waveguide by a one-dimensional transmission Fresnel-zone-plate (FZP) with its zones parallel to the waveguide plane. An example of such an FZP lens is shown in the scanning electron micrograph of Fig. 2. It consists of a rectangular pattern of trenches and ridges with a 50% duty cycle (trench-to-ridge ratio of 1:1) on a 5 μm -thick silicon membrane. The membrane was home-made by reactive ion etching (David, Ziegler & Nöhhammer, 2001). The width of the Fresnel zones (71 zone pairs in total) decreases away from the center and the outermost zone width d is 350 nm. The height h of the ridges is 5.5 μm . The lens aperture perpendicular to the ridges, D , equals 200 μm and that along the ridges 2.5 mm. The structure was patterned using electron-beam lithography and subsequently wet chemical etching. Details of the manufacture process are given by David, Ziegler & Nöhhammer (2001).

The focusing efficiency of the FZP lens depends on the shape and height of the zone-plate structures. For a structure with a rectangular profile and a 50% duty cycle, the first-order diffraction peak has a maximum theoretical collecting efficiency η_{lens}^1 given by (Kirz, 1974)

$$\eta_{\text{lens}}^1 = \pi^{-2} [1 + \exp(-2\varphi\beta/\delta) - 2\exp(-\varphi\beta/\delta) \cos(\varphi)], \quad (5)$$

where δ and β represent the real and imaginary part of the refractive index $n = 1 - \delta - i\beta$, respectively, and $\varphi = 2\pi h\delta/\lambda$ is the relative phase shift between the X-rays travelling through the ridges and those travelling through the trenches. The efficiency is at a maximum for $\varphi \simeq \pi$. In our case, the wavelength λ equals 0.0939 nm and the lens material is silicon, yielding $\delta_{\text{Si}} = 2.79 \times 10^{-6}$ and $\beta_{\text{Si}} = 2.44 \times 10^{-8}$. This gives an optimum zone height, h , of 16.8 μm , which is significantly larger than the fabricated structure height of 5.5 μm . However, by rotating the lens by an angle of 70.9° with respect to the X-ray beam (Fig. 1) we increase the effective path length h through the ridges to 16.8 μm . In this way, the lens can be

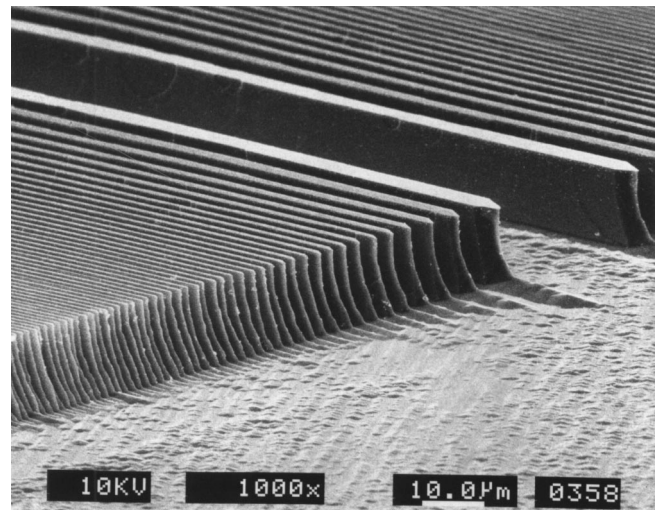


Figure 2 Scanning electron micrograph of the central part of a transmission Fresnel-zone-plate lens. The height of the structures forming the Fresnel zones is 5.5 μm .

$$J_5(\theta_i, x_5, x'_5) = A_5 \int_{\text{lens}} \int dx_2 dx'_2 \exp\left\{[-2\pi^2 \sigma_{0,v}^2 (x_2 - x'_2)^2] / (\lambda^2 R_{01}^2)\right\} \times E_5^p(\theta_i + x_2/R_{23}, x_5) E_5^{p*}(\theta_i + x'_2/R_{23}, x'_5), \quad (11)$$

where the integration boundaries are given by the lens aperture, the pre-factor $A_5 = A_0 4(2\pi)^{1/2} \sigma_{0,v} / (\lambda R_{01} R_{23})$, and R_{01} and R_{23} are the distances between the source and the lens and between the lens and the waveguide, respectively. The e.m. field $E_5^p(\theta_i + x_2/R_{23}, x_5)$ is the field in the detector at the point x_5 due to a plane wave of unit amplitude incident on the waveguide at an angle $\theta_i + x_2/R_{23}$. Therefore, the propagation of the partially coherent focused beam through the waveguide can be described by a combination of incident plane waves. Once the e.m. field $E_5^p(\theta_i, x_5)$ is numerically evaluated in the relevant range of incidence and exit angles (the exit angle $\theta_e \simeq x_5/R_{45}$), the mutual intensity function can be calculated for various source sizes $\sigma_{0,v}$. Since the numerical evaluations of the propagation of the e.m. field through the waveguide are very time consuming, this speeds up the analysis significantly. Lens defects are described statistically by multiplying the propagator $E_5^p(\theta_i + x_2/R_{23}, x_5)$ by a focusing-efficiency function $F(x_2)$.

We now discuss briefly the two extreme cases of complete incoherent and complete coherent illumination of the lens. In the limit of an infinitely large source, the lens is illuminated by fully incoherent radiation. The Gaussian function in (11), which is identical to the absolute value of the degree of coherence at the lens exit $|\mu_2(x_2, x'_2)|$, can then be replaced by $\lambda R_{01} (2\pi)^{-1/2} / \sigma_{0,v}$ times the Dirac delta function $\delta(x_2 - x'_2)$. This gives us the intensity distribution $I_5^{\text{incoh}}(\theta_i, x_5)$ in the detector plane for incoherent illumination of the lens,

$$I_5^{\text{incoh}}(\theta_i, x_5) = (4A_0/R_{23}) \int_{\text{lens}} dx_2 |E_5^p(\theta_i + x_2/R_{23}, x_5)|^2. \quad (12)$$

In the case of coherent illumination of the lens, the source size $\sigma_{0,v}$ can be set to zero and the intensity distribution $I_5^{\text{coh}}(\theta_i, x'_5)$ is given by

$$I_5^{\text{coh}}(\theta_i, x_5) = A_5 \int_{\text{lens}} \int dx_2 dx'_2 E_5^p(\theta_i + x_2/R_{23}, x_5) \times E_5^{p*}(\theta_i + x'_2/R_{23}, x'_5). \quad (13)$$

For coherent illumination of the lens, the interference effects between the different modes will be largest, and this will result in large intensity modulations in the diffraction patterns in the detector. In the case of incoherent illumination, the intensity modulations will be small.

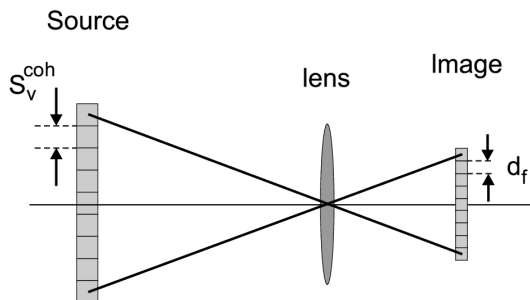


Figure 4
The source can be divided into small parts of size $s_{0,v}^{\text{coh}}$, such that every subsurface illuminates the lens coherently. A source of this size can be considered to be a point source and will have a fully coherent image. The size of this image is determined by the resolution of the lens d_f .

5. Experimental

The experiment was performed at the ID22 undulator beamline of the European Synchrotron Radiation Facility (ESRF) in Grenoble. The lens, the waveguide setup and the detectors were all positioned on a single granite optical table. This provided the necessary stability of the relative positions of the components. The distances between the lens and the source and the lens and the waveguide were $R_{01} = 40$ m and $R_{23} = 760$ mm, respectively. At these positions, the lens images the source height exactly onto the waveguide entrance with a magnification factor $M = R_{23}/R_{01} \simeq 1/52.6$. An adjustable horizontal slit was positioned in front of the lens to allow the lens aperture to be changed.

The energy of the X-rays was 13.2 keV ($\lambda = 0.0939$ nm), selected with an Si(111) double-crystal monochromator ($\Delta\lambda/\lambda = 1.4 \times 10^{-4}$). The effective vertical source size $\sigma_{0,v}$ of the undulator was experimentally determined from the visibility of the interference fringes resulting from diffraction off a thin boron fiber (Kohn *et al.*, 2000). We found $\sigma_{0,v} = 16$ (1) μm , which corresponds to a FWHM source size $s_{0,v} = 38$ (2) μm . The horizontal source size was $s_{0,h} \simeq 700$ μm (FWHM). The beam size at the lens was 0.5 mm along the vertical direction and 0.1 mm along the horizontal direction, defined by entrance slits in front of the lens.

The vertical and horizontal transverse coherence lengths at the lens position were $\xi_{1,v} \simeq 99$ μm and $\xi_{1,h} \simeq 5.4$ μm , respectively. If the lens was absent, the vertical and horizontal coherence lengths at the waveguide entrance were $\xi_{3,v} \simeq 101$ μm and $\xi_{3,h} \simeq 5.5$ μm , respectively.

For measurement of the total transmitted intensity through the waveguide as a function of the vertical lens position, a PIN diode was used. The PIN diode was positioned behind the waveguide and had an area large enough to capture all outgoing intensity. More detailed information is obtained from measurements of the diffracted far-field intensity distributions $I_5(\theta_i, \theta_e)$ as a function of both incidence angle θ_i and exit angle $\theta_e \simeq x_5/R_{45}$. For these measurements, a fluorescent screen 1180 mm from the exit of the waveguide converted the X-ray photons to a visible-light image that was recorded by a 12-bit cooled CCD camera (PCO Sensicam, 1024 \times 1280 pixels). The spatial resolution of this X-ray camera is ~ 10 μm , corresponding to an angular resolution of 0.5 millidegrees. Each CCD image records for one incidence angle θ_i the intensity $I_5(\theta_i, \theta_e)$ diffracted from the waveguide exit as a function of the vertical exit angle θ_e . By tilting the waveguide, we varied θ_i in steps of 0.001° , and we obtained the diffracted intensity distribution $I_5(\theta_i, \theta_e)$ as a function of both incidence and exit angle.

6. Results

6.1. Lens properties

We first discuss two specific lens properties: the focusing efficiency and the size of the source image created by the lens. To measure the focusing efficiency η_{lens}^1 of the first-order diffraction maximum of the zone-plate lens, we set the waveguide at a gap width of $W \simeq 6$ μm , much larger than the expected image width of $s_{3,v} = s_{0,v} M \simeq 0.72$ μm . This was to ensure that the complete image was captured by the waveguide entrance. The waveguide was positioned in the center of the beam and the total transmitted intensity $I(x)$ was measured as a function of the vertical lens position x . Thus, the focus of the first-order diffraction maximum was scanned over the entrance of the waveguide, which was tilted with respect to the beam at an angle $\theta_i = 0.02^\circ$, *i.e.* well below the critical angle $\theta_c = 0.125^\circ$ for the air-silica interface. The result is shown in Fig. 5.

The lens height is visible in Fig. 5 as the 200 μm -wide low-intensity area that has a central peak containing the flux of the first-order diffraction maximum. The background in the low-intensity area consists of other diffraction orders of the FZP lens. The width of the peak equals twice the waveguide width of 6 μm , because of the pre-reflection in front of the waveguide. The lens efficiency η_{lens}^1 is given by (David & Souvorov, 1999)

$$\eta_{\text{lens}}^1 = (D I_c)^{-1} \int_{\text{peak}} I(x) dx, \quad (14)$$

where D is the lens height, $I(x)$ is the total intensity transmitted through the waveguide as a function of the lens position and I_c is the total transmitted intensity with the lens taken out of the beam. From the data in Fig. 5 and the measured I_c we find an efficiency η_{lens}^1 of 32.6%. This is somewhat lower than the maximum theoretical focusing efficiency of 37.6% given in §3 for our one-dimensional zone-plate lens.

Next, we closed the gap to $W \simeq 244$ nm, smaller than the expected image size $s_{3,v} = 0.72$ μm , and we again scanned the vertical lens position. In this way, the waveguide is used as a narrow slit to determine the image profile. The measured transmitted intensity $I(x)$ is shown in Fig. 6. The FWHM of the measured peak equals 1.03 μm , which is larger than the expected image size $s_{3,v} \simeq 0.72$ μm because of the limited resolution of the lens and the integration over the gap width W . This is taken into account by first convoluting the 0.72 μm -wide Gaussian image profile with a $[\sin(ax)/ax]^2$ function with the first zero at $x = d_f = 0.35$ μm , which represents the shape of the image of a point source. This results in an image FWHM of 0.78 μm . Subsequently, we convolute the obtained image profile with a square transmission function of width 0.488 μm , which is twice the waveguide gap. The doubled width of the transmission function is a consequence of the pre-reflection in front of the waveguide. We find an expected experimental image width of 0.84 μm (dash-dotted line in Fig. 6), still somewhat smaller than the measured 1.03 μm .

The maximum intensity in Fig. 6 is a gain factor $G = 54$ larger than the transmitted intensity with the lens taken out of the beam. This flux enhancement in the waveguide by almost two orders of magnitude will allow for new types of experiments on confined geometries such as photon correlation spectroscopy.

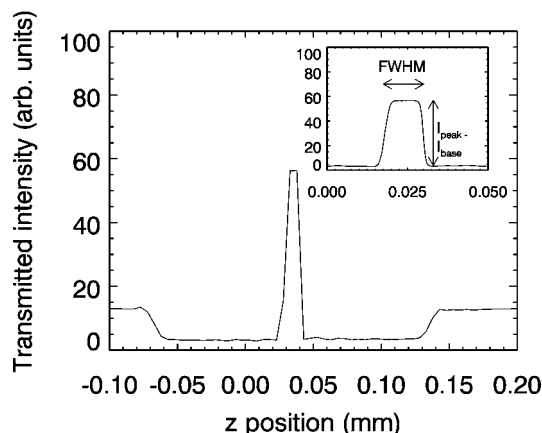


Figure 5
The measured total transmitted intensity through a waveguide with a gap width $W \simeq 6$ μm as a function of the vertical lens position. The inset shows a finer scan of the central peak. From the integrated intensity of the peak, we derive a lens-collecting efficiency of 32.6% (see text).

The fact that the measured efficiency is somewhat lower than the theoretical value and that the image profile is broader than theoretically expected suggests that there are imperfections in the lens structure. Most likely, the imperfections are in the delicate outer zones, which determine the resolving power of the lens. Also, a small misalignment in the vertical tilt angle of the lens would result in a lower performance of the lens. Such a tilt changes the position-dependent phase shift $\varphi(x)$ and thereby reduces the lens efficiency. Another explanation might be that the focal spot is at a slightly different z position for different parts of the lens owing to its tilt angle. The z position changes by 0.3 mm at the tilt angle used here. However, this change is much smaller than the focal depth, given by $2d^2/\lambda \simeq 2.6$ mm. The latter was confirmed by a measurement of the focal width at varying z positions around the focal spot. From this we conclude that the observed broadening is not explained by defocusing, due to the tilt angle of the lens, but mostly by small lens imperfections and a small misalignment of the lens.

Further improvements in the lens quality and alignment would enhance the gain. In the optimal case, the flux incident on the lens multiplied by the maximum efficiency of the lens η_{lens}^1 would be completely focused into a Gaussian-shaped image with a FWHM of $s_{3,v} = 0.78$ μm (standard deviation $\sigma_{3,v} = 0.33$ μm). This yields a maximum theoretical gain $G = D\eta_{\text{lens}}^1(2\pi)^{-1/2}/\sigma_{3,v} = 80$ if the gap width W is much smaller than the image size $s_{3,v} = 0.78$ μm .

6.2. Propagation of a partially coherent beam through the waveguide

Focusing the beam results in a larger angular distribution of the beam and also affects the spatial coherence of the beam at the position of the waveguide, as mentioned in §4. Furthermore, defects in the lens may have undesirable effects on the beam profile and the coherence. These effects are observable in the far-field diffraction patterns $I_5(\theta_1, \theta_c)$.

We first set the waveguide at a relatively large gap width of $W \simeq 1$ μm . The mode spacing $\Delta\theta = \lambda/(2W)$ equals 0.0027° for this

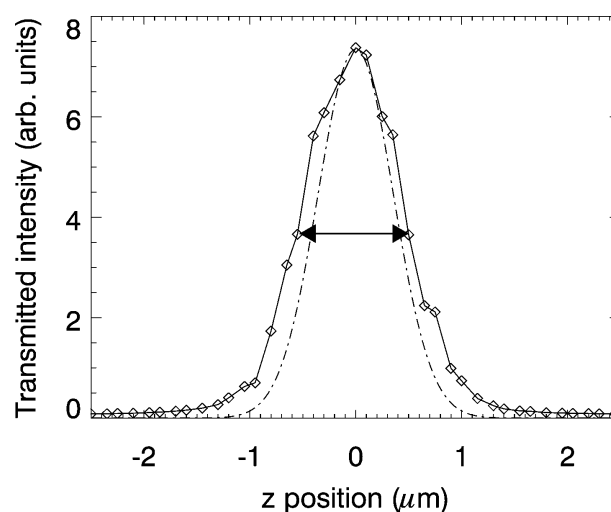


Figure 6
The measured total transmitted intensity (diamonds connected by lines) through the waveguide as a function of the vertical lens position for a waveguide gap width $W = 244$ nm. The FWHM of the peak, depicted by the arrow, is 1.03 μm and the peak intensity is a factor of 54 higher than that with the lens completely removed. The dash-dotted line is a Gaussian curve of 0.84 μm FWHM, indicating the width of the optimal theoretical curve.

gap, which is a factor of 5.5 smaller than the convergence angle of the focused beam $\Delta\Omega = D/R_{23} = 0.015^\circ$. This should result in the simultaneous excitation of five to six modes in the presence of the lens. Also, the coherence angle of the incident converging beam, given by $\xi_{1,v}/R_{23} \simeq 0.0075^\circ$, is of the order of a few mode spacings. By studying the interference of the modes we obtain information about the coherent properties of the focused beam.

Fig. 7(a) shows a contour plot of the intensity distribution $I_5(\theta_i, \theta_e)$, measured in the absence of the lens. At angles of incidence at which the intensity has a maximum along the diagonal, the standing-wave pattern at the entrance is matched to one of the waveguide modes and only a single mode is excited. The dash-striped pattern along the diagonal is a result of multi-mode interference of neighboring modes that are excited simultaneously at angles in between mode angles (Zwanenburg *et al.*, 1999). The modes interfere either constructively or destructively for $\theta_e = \theta_i$, depending on both the waveguide length and the mode angles θ_m . From the angular mode spacings in Fig. 7(a), the gap width W was accurately determined at $W = 1090$ nm.

We numerically simulated the measurements of the far-field diffraction patterns $I_5(\theta_i, \theta_e)$ using the beam propagation method (Scarmozzino & Osgood, 1991) and thus obtained the e.m. field

pattern $E_5^p(\theta_i, \theta_e)$ in the detector for incident plane waves (*i.e.* no lens inserted). The beam propagation calculations were performed on a Unix-based platform using a program written in C++ based on the light numerical recipes library (see Ladouceur, 2002). Fig. 7(b) shows the numerically calculated intensity distribution $I_5(\theta_i, \theta_e)$ without lens for a waveguide gap $W = 1090$ nm and a waveguide length $R_{34} = 5.5$ mm. The agreement between the calculated and measured diffraction patterns $I_5(\theta_i, \theta_e)$ (Figs. 7a and 7b) is excellent, which demonstrates the plane-wave character and the coherence of the incident unfocused beam. The differences between Figs. 7(a) and 7(b) at angles close to zero are caused by the finite size of the lower surface both in front of and at the exit of the waveguide in the experiment. The lower surface is too small to result, at small angles, in a standing-wave pattern covering the entire waveguide gap.

Fig. 8 shows the measured and calculated far-field diffraction patterns for one angle of incidence $\theta_i = 0.039^\circ$. Again, the agreement between calculation and experiment is good, but the minima in between the maxima are slightly deeper in the calculation than in the experiment. This is caused by small imperfections of the waveguide surfaces, which result in a filling of the minima. The surface imperfection can be roughness, slope error or a combination of both.

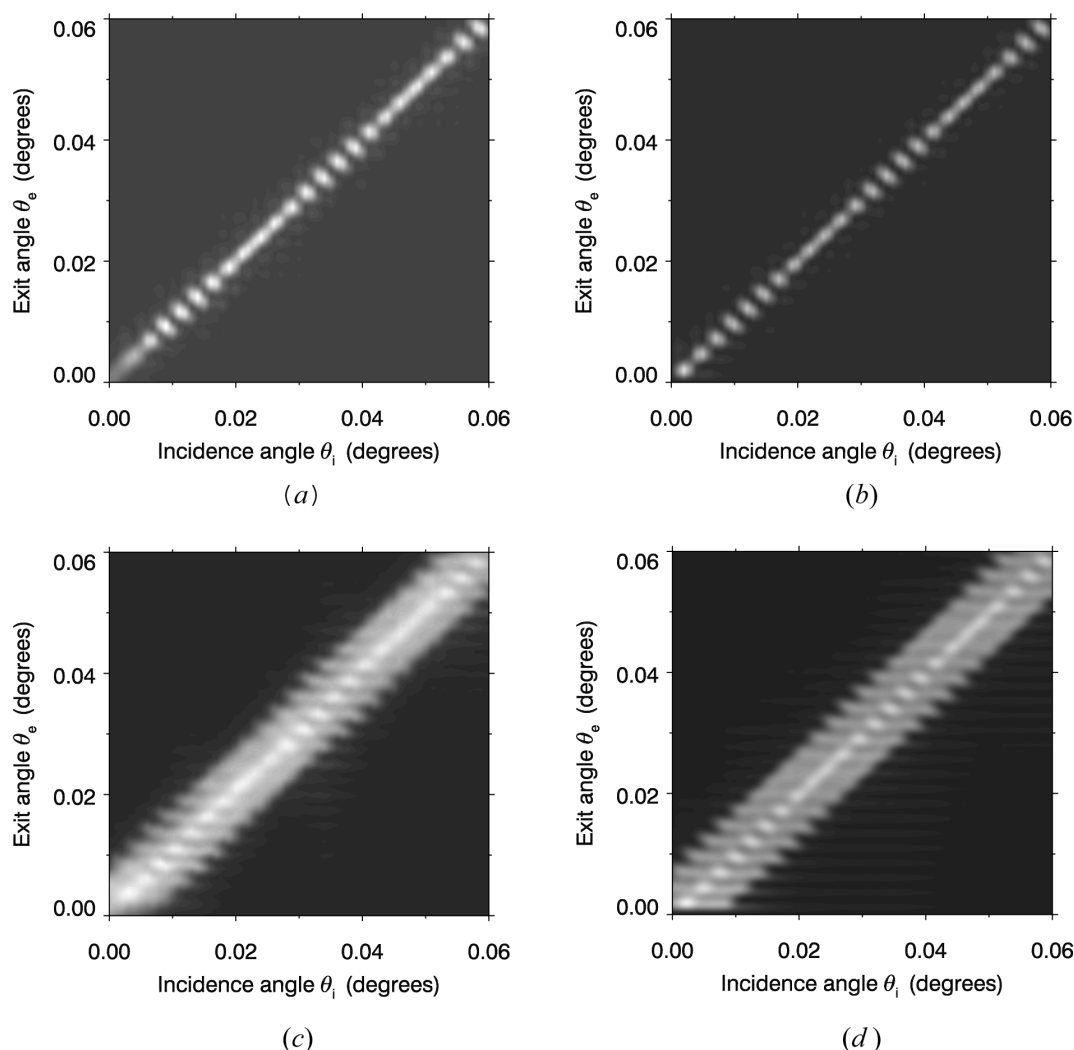


Figure 7

Contour plots of the far-field intensity distributions $I_5(\theta_i, \theta_e)$ as a function of the incidence and exit angles θ_i and θ_e . The gap width is given by $W = 1090$ nm and the waveguide length by $R_{34} = 5.5$ mm. (a) Experimental data, without lens; (b) numerical calculation, without lens; (c) experimental data, with lens; (d) numerical calculation, with lens.

Next, we inserted the lens in the beam and repeated the measurement of $I_5(\theta_i, \theta_e)$. The result is shown in Fig. 7(c). The diagonal is now much broader than in Fig. 7(a), which reflects the angular range of the converging cylindrical wave in the focused beam. We find an angular width of $\Delta\Omega \simeq 0.015^\circ$, identical to the expected angular range.

We now apply (11) to calculate $I_5(\theta_i, \theta_e)$ for the case where the lens is inserted, using the numerically calculated e.m. field $E_5^p(\theta_i, \theta_e)$ for incident plane waves. The lower focusing efficiency of the outer Fresnel zones is taken into account by multiplying the e.m. field $E_5^p(\theta_i + x_2/R_{23}, \theta_e)$ for incident plane waves by a 200 μm -wide (FWHM) square transmission profile $F(x_2)$, the rounded edges of which gradually decrease from 1 to 0 within 20 μm .

We also take into account the fact that a Fresnel-zone-plate lens with a rectangular profile has many diffraction orders, of which the first is just the dominant one. Moreover, for every positive focusing order there is a negative defocusing order. For all diffraction orders other than the first order, the waveguide is out of focus and the beam

has expanded at the waveguide position to a size much larger than the waveguide gap W . Therefore, only a small part enters the waveguide. This is shown in Fig. 9 for the positive and negative first-order diffraction maxima. Most of the first diffraction order will enter the 1 μm -wide waveguide, while of the negative order only a small fraction is captured by the waveguide. The angular distribution of these captured waves is much smaller than the mode spacing, and they can be treated as single plane waves. Since this holds for all other diffraction orders as well, they are indistinguishable from each other in the diffraction patterns and we will treat the contributions of all other orders collectively as a plane-wave background.

The plane-wave background is included in the calculations by adding to the propagator $E_5^p(\theta_i + x_2/R_{23}, x_5)$, used in (11), a plane-wave contribution only for the case $x_2 = 0$. We then have a new propagator $E_5^{\prime p}(\theta_i + x_2/R_{23}, x_5)$, given by

$$E_5^{\prime p}(\theta_i + x_2/R_{23}, x_5) = E_5^p(\theta_i + x_2/R_{23}, x_5) + B\delta(x_2)E_5^p(\theta_i + x_2/R_{23}, x_5), \quad (15)$$

where $\delta(x)$ is the Dirac delta function and $B\delta(x_2)$ is the amplitude of the plane-wave background. Fig. 10 shows the measured and calculated diffraction patterns for one incidence angle $\theta_i = 0.039^\circ$. The relative intensity of the plane-wave background, given by B^2/D^2 , was 0.1% in the calculation. The effect of the plane-wave background on the diffraction pattern is larger than this relative intensity owing to the interference term in $E_5^{\prime p}E_5^{\prime p*}$. The best agreement between experiment and calculation is obtained if an effective source size $s_{0,v} = 76 \mu\text{m}$ is assumed, twice the value given earlier in §5. Since the FZP lens and the waveguide are the only added components compared with the experiment with the boron fiber from which the source size was determined earlier, they must be the origin of the enhanced effective source size. In the case without the lens (Fig. 8), we observed small deviations from the calculations caused by imperfect surfaces of the waveguide. In the experiment with the lens inserted, multiple modes are excited simultaneously and the observed intensity modulations are more sensitive to the roughness or slope

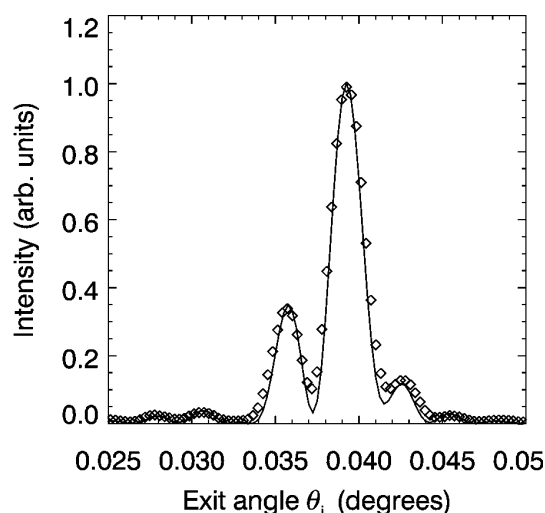


Figure 8
Far-field diffraction pattern $I_5(\theta_i, \theta_e)$ in the absence of the lens for incidence angle $\theta_i = 0.039^\circ$. The diamonds are the experimental data; the solid line represents the numerical calculation for an incident plane wave. The waveguide gap is 1090 nm, its length 5.5 mm.

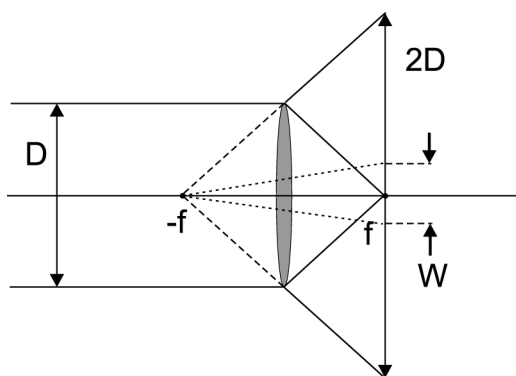


Figure 9
The first-order diffraction maximum of the FZP lens creates a small focus at the focal point. The first-order diffraction maximum results in a broad intensity distribution of size $2D$ at the focal spot. The waveguide of width W only captures a fraction W/D of this flux (doubled because of the pre-reflection), and the angular distribution of these waves has a width of W/f .

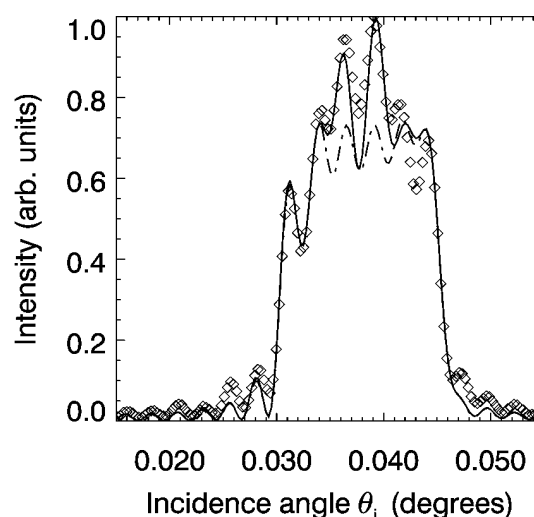


Figure 10
Outgoing intensity distribution $I_5(\theta_i, \theta_e)$, in the presence of the lens, for one angle of incidence $\theta_i = 0.039^\circ$. The measured data are represented by diamonds and the calculated intensity profile, taking into account a plane-wave background, by the solid line, and the dashed line is the curve calculated without plane-wave background. The waveguide gap is 1090 nm, its length 5.5 mm.

error of the surfaces, resulting in an enhanced effective source size. The lens also has an effect on the effective source size, but its enhancement cannot be explained by lens effects alone. If the enhanced source size was only caused by the lens, a larger image size $s_{3,v} = 76 \mu\text{m} \times M = 1.46 \mu\text{m}$ would have been observed in Fig. 6.

Fig. 7(d) shows a contour plot of the calculated diffraction patterns $I_5(\theta_i, \theta_e)$ in the presence of the lens. There is a large similarity with the experimental data in Fig. 7(c), both in the amplitude of the intensity oscillations on the diagonal and in the narrow band of higher intensity on the diagonal. The good agreement proves that the approximation of the FZP lens by a perfect phase-shifting lens and a plane-wave background is justified.

As discussed in §4, the beam becomes partially incoherent on the length scale of the waveguide gap of $1 \mu\text{m}$ when the lens is inserted. For some experiments, however, a fully coherent beam is required. The coherence of the beam can be restored in two ways. Either the coherence length at the sample is enhanced or the sample size is reduced. The former is achieved by reducing the vertical lens aperture using an adjustable horizontal slit in front of the lens (see Fig. 3). In the extreme case of closing down the lens aperture to an aperture significantly smaller than the vertical coherence length $\xi_{1,v} \simeq 99 \mu\text{m}$, the lens is illuminated by a coherent beam, which results in a coherent image at the waveguide, irrespective of its gap width W . Fig. 11 shows the far-field diffraction patterns after the waveguide for three different lens apertures ($\theta_i = 0.039^\circ$ and $W = 1090 \text{ nm}$). The upper curve corresponds to full illumination of the lens with an aperture of $200 \mu\text{m}$. The other curves correspond to a lens aperture of $100 \mu\text{m}$ (middle) and $25 \mu\text{m}$ (bottom). As the aperture is decreased, fewer modes are excited and the intensity modulations become larger. These larger modulations are a result of the enhanced degree of coherence of the beam. At an aperture of $25 \mu\text{m}$, the diffraction pattern is identical in shape to the curve for an incident plane wave, corresponding to fully coherent illumination of the waveguide. The differences between the lowest curves in Figs. 11 and 8 are caused by a small misalignment of the optical axis of the lens, which caused a deviation in the incidence angle θ_i . Fig. 11 demonstrates that the coherence is maintained at a reduced lens aperture and a large gap

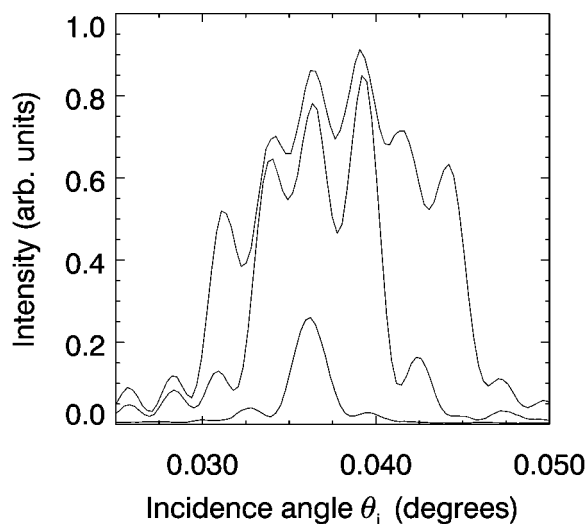


Figure 11
The outgoing intensity distribution for an incidence angle $\theta_i = 0.039^\circ$ at different lens apertures. The upper curve corresponds to an aperture of $200 \mu\text{m}$ (full illumination of the lens), the middle curve to an aperture of $100 \mu\text{m}$ and the lower curve to an aperture of $25 \mu\text{m}$.

width $W = 1090 \text{ nm}$, while the intensity is a factor of two higher than the intensity for the unfocused beam. The lower gain factor here, compared with the value of 54 given earlier, is not surprising and is caused by the convolution of the image of the source with a larger square transmission profile of width $2.18 \mu\text{m}$, the smaller lens aperture and the fact that the FZP-lens efficiency is lower at an aperture of $25 \mu\text{m}$ because of the lower number of exposed Fresnel zones. At smaller gaps these effects are more favorable and the gain factor for coherent excitation of the waveguide modes is higher.

The second way to enhance the coherence of the beam on the sample is by decreasing the sample size to a value equal to or smaller than the vertical coherence length in the focus, which is given by the outermost zone width d (see Fig. 4). Now, the number of photons on the sample decreases with the sample size, but the flux gain caused by the introduction of the lens remains unchanged. In Fig. 12, the measured intensity distribution $I_5(\theta_i, \theta_e)$ is shown for a waveguide with a small gap and with a pre-focused beam. The upper surface is slightly tilted, such that the entrance gap $W_1 = 238 \text{ nm}$ and the exit gap $W_2 = 191 \text{ nm}$. The waveguide at the entrance is now of the order of the local coherence length $\xi_{3,v}$. Except for the flux enhancement, the plot is similar to the plot without the lens (not shown here), with only excited modes on the diagonal $\theta_e = \theta_i$. The condition for excitation of single modes, $\Delta\Omega < \Delta\theta$, can be rewritten using $\Delta\Omega = D/f$, which gives $W < d/2$, half the coherence length of the focused beam at the waveguide entrance. Therefore, the observation that single modes are excited in the presence of the lens is a good indication of the coherence of the beam. Note, though, that this argumentation is not valid when inverted. Excitation of multiple modes does not necessarily mean that the beam is incoherent.

7. Conclusions

We have demonstrated the use of a one-dimensional Fresnel-zone-plate lens for focusing a hard X-ray beam onto the entrance of a planar X-ray waveguide. The achieved flux enhancement by a factor of 54 makes it possible to perform, for example, X-ray photon correlation spectroscopy studies of the dynamical properties of confined fluids. The propagation of a partially coherent focused beam through a waveguide can be described adequately by classical wave

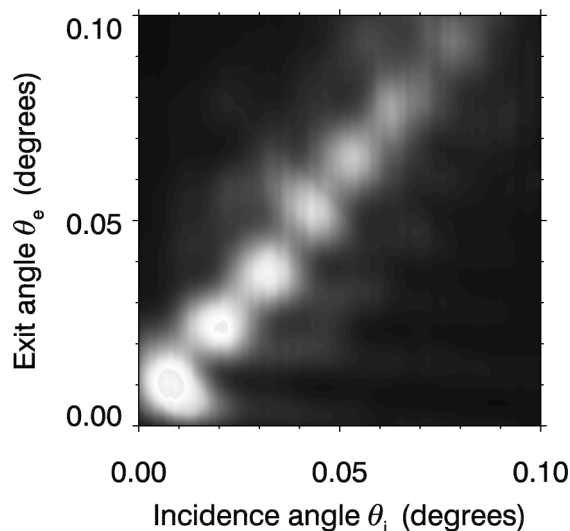


Figure 12
The intensity distribution $I_5(\theta_i, \theta_e)$ with the lens inserted and a waveguide gap of width $W_1 = 237.7 \text{ nm}$ at the entrance and of width $W_2 = 190.8 \text{ nm}$ at the exit.

optics, as described in §4 and Appendix A. The approximation of the FZP lens by a perfect lens with a low-intensity plane-wave background proves to be sufficient to explain the observed diffraction patterns.

If a spatially coherent beam is required, one has to ascertain that the coherence is not destroyed by the lens on the length scales of the sample. A trade-off has to be made between flux enhancement and preservation of coherence. As demonstrated above, the coherence length can be tuned in two ways. We can adjust the aperture of the lens such that the coherence length at the sample is larger than the sample itself. However, by reducing the lens aperture, the flux gain is reduced. The focusing properties of the lens are more fully employed, with conservation of coherence, if the sample is made smaller than the coherence length in the focus. This is, however, not always possible and depends on the specific experimental conditions.

In the case that coherence is not required and just flux enhancement is desired, the lens diameter can be enlarged so that more flux is captured in the lens aperture. To keep the same demagnification factor, however, one then needs a smaller outermost zone width, which may be beyond the limit of what is technically possible.

The observed effective source size with the lens and the waveguide inserted is twice the size observed without these two optical components. Seemingly, the coherence of the beam is affected by defects and roughness of these two components. We have demonstrated, however, that coherent propagation of waveguide modes in the waveguide is possible with a pre-focused beam.

So far, we have paid no attention to the fact that the lens affects the angular resolution of diffraction experiments in which the scattering vector is along the focusing direction. If the convergence angle $\Delta\Omega$ of the incident beam is larger than the angular mode spacing $\Delta\theta$ and the modes are excited incoherently, the angular resolution is given by the angle $\Delta\Omega$, and thus the angular resolution is reduced. For coherent excitation of the modes, it should, in principle, be possible to deconvolve the convergence angle from the diffraction data, but this significantly complicates the analysis. If one investigates the in-plane (the non-focusing direction) structure or dynamics, this disadvantage is, of course, absent.

In the future, we will perform XPCS studies on fluids confined within the waveguide using a pre-focused coherent X-ray beam. The considerations presented in this paper will contribute to these experiments because they define the optical parameters for flux enhancement at preserved transverse coherence of the beam.

APPENDIX A Propagation of the mutual intensity function

If the mutual intensity function $J_i(\mathbf{x}_i, \mathbf{x}'_i)$ at one plane in space S_i , perpendicular to the propagation direction, is known, its propagation to a different plane S_j is calculated *via*

$$J_j(\mathbf{x}_j, \mathbf{x}'_j) = \iint d\mathbf{x}_i d\mathbf{x}'_i J_i(\mathbf{x}_i, \mathbf{x}'_i) K_{ij}(\mathbf{x}_i, \mathbf{x}_j) K_{ij}^*(\mathbf{x}'_i, \mathbf{x}'_j), \quad (16)$$

where $K_{ij}(\mathbf{x}_i, \mathbf{x}_j)$ is the transmission function describing the disturbance at $\mathbf{x}_j = (x_j, y_j)$ in plane S_j due to a disturbance at $\mathbf{x}_i = (x_i, y_i)$ in plane S_i , and K_{ij}^* is the complex conjugate of K_{ij} . Here, we describe the propagation of the mutual intensity function from the source to the lens and *via* the waveguide to the detector (see Fig. 3).

Since we are considering diffraction effects only in the vertical x direction, and the source is much larger in the y than in the x direction, we assume the source to be infinite in the horizontal y direction. The propagation can then be completely described using

cylindrical waves in x and z coordinates only. The propagator K_{ij}^c for the cylindrical wave through free space is given by (Cowley, 1995)

$$K_{ij}^c(x_i, x_j) = [i/(s_{ij}\lambda)]^{1/2} \exp(iks_{ij}), \quad (17)$$

where s_{ij} is the distance between x_i and x_j . For $|x_i|, |x_j| \ll s_{ij}$ we have

$$K_{ij}^c(x_i, x_j) \simeq [i/(R_{ij}\lambda)]^{1/2} \exp(ikR_{ij}) \exp[ik(x_i - x_j)^2/(2R_{ij})], \quad (18)$$

where R_{ij} is the distance from plane S_i to plane S_j .

The X-ray source is in our case the insertion device in the electron storage ring and is considered to be spatially fully incoherent. For an incoherent source, (16) becomes (Born & Wolf, 1980)

$$J_j(\mathbf{x}_j, \mathbf{x}'_j) = \lambda^2 \int d\mathbf{x}_i I_s(\mathbf{x}_i) K_{ij}(\mathbf{x}_i, \mathbf{x}_j) K_{ij}^*(\mathbf{x}'_i, \mathbf{x}'_j), \quad (19)$$

where $I_s(\mathbf{x}_i)$ is the intensity distribution of the source. The equivalent expression for cylindrical waves is

$$J_j(x_j, x'_j) = \lambda \int dx_i I_s(x_i) K_{ij}^c(x_i, x_j) K_{ij}^{c*}(x'_i, x'_j). \quad (20)$$

From now on, we will omit the superscript c in K_{ij}^c , and the propagator K_{ij} will always be a propagator of cylindrical waves.

We assume a Gaussian intensity profile $I_s(x_0)$ for the source,

$$I_s(x_0) = A_0 \exp[-x_0^2/(2\sigma_{0,v}^2)], \quad (21)$$

where $\sigma_{0,v}$ represents the vertical source size. The FWHM of the source $s_{0,v} = 2[2 \ln(2)]^{1/2} \sigma_{0,v}$. We then obtain the mutual intensity function $J_1(x_1, x'_1)$ at the entrance plane S_1 of the lens:

$$\begin{aligned} J_1(x_1, x'_1) &= A_0 \lambda \int dx_0 \exp[-x_0^2/(2\sigma_{0,v}^2)] K_{01}(x_0, x_1) K_{01}^*(x'_0, x'_1) \\ &= A_1 \exp[ik(x_1^2 - x'^2_1)/(2R_{01})] \\ &\quad \times \exp\{-\pi^2(x_1 - x'_1)^2/[4 \ln(2) \xi_{1,v}^2]\} \\ &= A_1 \mu_1(x_1, x'_1), \end{aligned} \quad (22)$$

where R_{01} is the distance from the source to the lens, $A_1 = A_0 \sigma_{0,v} (2\pi)^{1/2} / R_{01}$ and $\xi_{1,v}$ is the vertical coherence length at the lens, given by $\xi_{1,v} = \lambda R_{01} / s_{0,v}$. In the last line of (22) we introduced the complex degree of coherence $\mu_i(x_i, x'_i)$, which for plane S_i is defined as

$$\mu_i(x_i, x'_i) = J_i(x_i, x'_i) [I_i(x_i)]^{-1/2} [I_i(x'_i)]^{-1/2}. \quad (23)$$

The mutual intensity function at the exit pupil of the lens is given by

$$J_2(x_2, x'_2) = J_1(x_1 = x_2, x'_1 = x'_2) \exp\{i[\varphi(x_2) - \varphi(x'_2)]\}, \quad (24)$$

where $\varphi(x)$ is the phase shift caused by the lens. We assume that the lens is a pure phase object and neglect absorption. For the Fresnel lens, the phase shift equals zero or π , depending on whether the vertical lens position x corresponds to a ridge or a trench in the zone-plate profile. However, in the following we will consider a perfect lens, since it is less involved both in notation and in calculation. The phase shift for a perfect lens is found using Fermat's principle of shortest optical path. This gives

$$\varphi(x) = -kx^2(R_{01}^{-1} + R_{23}^{-1})/2, \quad (25)$$

where R_{01} is the distance between the source and the lens and R_{23} the distance between the lens and the image. For a perfect lens we then have

$$J_2(x_2, x'_2) = A_2 \exp\left[\frac{-ik(x_2^2 - x'^2_2)}{2R_{23}}\right] \exp\left[\frac{-\pi^2(x_2 - x'_2)^2}{4 \ln(2) \xi_{1,v}^2}\right], \quad (26)$$

with $A_2 = A_1$.

Next, we propagate $J_2(x_2, x'_2)$ through free space to the image plane S_3 , which is located at the entrance of the waveguide. We now have to

take into account the pre-reflection from the lower surface, which is tilted by an angle θ_1 with respect to the incident beam. The corresponding propagator $K_{23}(\theta_1, x_2, x_3)$ is given by

$$K_{23}(\theta_1, x_2, x_3) = \left(\frac{i}{\lambda}\right)^{1/2} \left\{ \frac{\exp(iks_{23})}{(s_{23})^{1/2}} + \frac{\exp[i\varphi(\theta)] \exp(iks_{23}^r)}{(s_{23}^r)^{1/2}} \right\}, \quad (27)$$

where s_{23} is the distance from x_2 to x_3 directly, s_{23}^r is the distance from x_2 to x_3 via the pre-reflection from the lower surface (see Fig. 3) and $\varphi(\theta)$ is the phase shift at reflection at the angle $\theta \simeq \theta_1 + (x_2 - x_3)/R_{23}$. The zeros for x_2 and x_3 are at the lens center and waveguide lower surface, respectively. For simplicity, we take a constant phase shift $\varphi = \pi$ at reflection. In the limit $x_2/R_{23}, x_3/R_{23}, \theta_1 \ll 1$, we obtain:

$$K_{23}(\theta_1, x_2, x_3) = 2i(i)^{1/2}(\lambda R_{23})^{-1/2} \exp(ikR_{23}) \exp[ik(x_2^2 + x_3^2)/(2R_{23})] \times \sin[kx_3(\theta_1 + x_2/R_{23})]. \quad (28)$$

This e.m. field propagates through the waveguide as described by (4). The propagator $K_{24}(\theta_1, x_2, x_4)$ between the planes S_2 and S_4 at the exit of the waveguide is given by

$$K_{24}(\theta_1, x_2, x_4) = \sum_m^{m_{\max}} c_m(\theta_1 + x_2/R_{23}) \psi_m(x_4) \exp(-i\beta_m R_{34}), \quad (29)$$

where R_{34} is the length of the waveguide, ψ_m is the mode profile of mode TE_m , given by (2), and the mode amplitudes c_m are given by

$$c_m(\theta_1 + x_2/R_{23}) = \int_{-\infty}^{+\infty} dx_3 K_{23}(\theta_1, x_2, x_3) \psi_m(x_3) = (2/W)^{1/2} 2i(i)^{1/2}(\lambda R_{23})^{-1/2} \times \exp(ikR_{23}) \exp[ikx_2^2/(2R_{23})] \times \int_0^W dx_3 \sin[kx_3(\theta_1 + x_2/R_{23})] \sin(kx_3\theta_m). \quad (30)$$

In the second line we have omitted the factor $\exp[ikx_3^2/(2R_{23})] \simeq 1$ from the integral, since $x_3 \ll R_{23}$. The mode amplitude $c_m(\theta_1 + x_2/R_{23})$ of mode TE_m , resulting from a cylindrical wave starting at the point x_2 , is, apart from a complex pre-factor, equal to the amplitude $c_m^p(\theta_1 + x_2/R_{23})$ for a plane wave incident at an angle $\theta_1 + x_2/R_{23}$. The latter amplitude is given by

$$c_m^p(\theta_1 + x_2/R_{23}) = (2/W)^{1/2} \int_0^W dx_3 \sin[kx_3(\theta_1 + x_2/R_{23})] \sin(kx_3\theta_m). \quad (31)$$

Hence,

$$c_m(\theta_1 + x_2/R_{23}) \simeq 2i(i)^{1/2}(\lambda R_{23})^{-1/2} \exp(ikR_{23}) \exp[ikx_2^2/(2R_{23})] \times c_m^p(\theta_1 + x_2/R_{23}). \quad (32)$$

The mutual intensity function $J_4(\theta_1, x_4, x_4)$ at the exit of the waveguide is given by

$$J_4(\theta_1, x_4, x_4) = \iint dx_2 dx_2' J_2(x_2, x_2') K_{24}(\theta_1, x_2, x_4) K_{24}^*(\theta_1, x_2', x_4). \quad (33)$$

The mutual intensity function in the detector plane S_5 is found by propagating $J_4(x_4, x_4)$, taking into account a post-reflection with a propagator as in (28). Now s_{23} and s_{23}^r are replaced by s_{45} and s_{45}^r , which are the distances from x_4 to x_5 directly and via a post-reflection, respectively. In the detector plane, we choose the zero of x_5 to be in the plane parallel to the lower surface. We then have

$$K_{45}(x_4, x_5) = 2i(i)^{1/2}(\lambda R_{45})^{-1/2} \exp(ikR_{45}) \exp[ik(x_4^2 + x_5^2)/(2R_{45})] \times \sin(kx_4x_5/R_{45}). \quad (34)$$

This results in the following mutual intensity function $J_5(x_5, x_5')$ in the detector plane,

$$J_5(\theta_1, x_5, x_5') = \iint dx_4 dx_4' J_4(\theta_1, x_4, x_4') K_{45}(x_4, x_5) K_{45}^*(x_4', x_5') = A_5 \iint dx_2 dx_2' \exp[-2\pi^2\sigma_{0,v}^2(x_2 - x_2')^2/(\lambda^2 R_{01}^2)] \times E_5^p(\theta_1 + x_2/R_{23}, x_5) E_5^{p*}(\theta_1 + x_2'/R_{23}, x_5'), \quad (35)$$

where the intensity $A_5 = A_0 4(2\pi)^{1/2} \sigma_{0,v}/(\lambda R_{01} R_{23})$. The second line in (35) is found by changing the order of integration. Now, the e.m. field in the detector at the point x_5 due to a plane wave of unit amplitude incident at an angle $\theta_1 + x_2/R_{23}$ is given by

$$E_5^p(\theta_1 + x_2/R_{23}, x_5) = 2i(i)^{1/2}(\lambda R_{45})^{-1/2} \exp(ikR_{45}) \times \int dx_4 \exp[ik(x_4^2 + x_5^2)/(2R_{45})] \sin(kx_4x_5/R_{45}) \times \left[\sum_m^{m_{\max}} c_m^p(\theta_1 + x_2/R_{23}) \psi_m(x_4) \exp(-i\beta_m R_{34}) \right]. \quad (36)$$

Writing $J_5(\theta_1, x_5, x_5')$ as in (35) is convenient because the e.m. fields $E_5^p(\theta_1, x_5)$ have to be calculated only once for all combinations of θ_1 and x_5 and the mutual intensity function in the detector may then be calculated for various source sizes $\sigma_{0,v}$. The intensity in the detector is given by $I_5(\theta_1, x_5) = J_5(\theta_1, x_5, x_5)$.

We may include in the calculations a position-dependent focusing efficiency $F(x_2)$ of the lens. This function describes possible defects of the lens in a simple way. The efficiency function is inserted by multiplying the MIF $J_2(x_2, x_2')$ at the exit of the lens by $F(x_2)F^*(x_2')$. We then have

$$J_5(\theta_1, x_5, x_5') = A_5 \iint dx_2 dx_2' \exp[-2\pi^2\sigma_{0,v}^2(x_2 - x_2')^2/(\lambda^2 R_{01}^2)] F(x_2) \times F^*(x_2') E_5^p(\theta_1 + x_2/R_{23}, x_5) E_5^{p*}(\theta_1 + x_2'/R_{23}, x_5'). \quad (37)$$

We thank I. Snigireva, M. de Vries and Y. Nahmad for their contributions to the experiment and the ID15 team of ESRF for the use of the Sensicam X-ray camera. This work was part of the research program of the Foundation of Fundamental Research on Matter (FOM) and was made possible by financial support from the Netherlands Organization for Scientific Research (NWO).

References

- Bongaerts, J. H. H., Zwanenburg, M. J., Zontone, F. & van der Veen, J. F. (2001). *J. Appl. Phys.* **90**, 94–100.
- Born, M. & Wolf, E. (1980). *Principles of Optics*. Oxford: Pergamon Press.
- Cowley, J. M. (1995). *Diffraction Physics*, 3rd ed., pp. 17–22. Amsterdam: North-Holland.
- David, C., Nöhhammer, B. & Ziegler, E. (2001). *Appl. Phys. Lett.* **79**, 1088.
- David, C. & Souvorov, A. (1999). *Rev. Sci. Instrum.* **70**, 4168–4173.
- David, C., Ziegler, E. & Nöhhammer, B. (2001). *J. Synchrotron Rad.* **8**, 1054–1055.
- Di Fonzo, S., Jark, W., Lagomarsino, S., Giannini, C., De Caro, L., Cedola, A. & Mueller, M. (2000). *Nature (London)*, **403**, 638–640.
- Feng, Y. P., Sinha, S. K., Deckman, H. W., Hastings, J. B. & Siddons, D. P. (1993). *Phys. Rev. Lett.* **71**, 537.
- Feng, Y. P., Sinha, S. K. & Fullerton, E. E. (1995). *Appl. Phys. Lett.* **60**, 3647.
- Jark, W., Di Fonzo, S., Lagomarsino, S., Cedola, A., Di Fabrizio, E., Bram, A. & Riekel, C. (1996). *J. Appl. Phys.* **80**, 4831.
- Kirz, J. (1974). *J. Opt. Soc. Am.* **64**, 301–309.
- Kohn, V., Snigireva, I. & Snigirev, A. (2000). *Phys. Rev. Lett.* **85**, 2745.
- Ladouceur, F. (2002). *Inr: Beam Propagation*, <http://www.rsfphyssce.anu.edu.au/~fjl124/web/bpm/bpm.html>.
- Lagomarsino, S., Cedola, A., Cloetens, P., Di Fonzo, S., Jark, W., Soullie, G. & Riekel, C. (1997). *Appl. Phys. Lett.* **71**, 2557.

- Lagomarsino, S., Jark, W., Di Fonzo, S., Cedola, A., Mueller, B., Engstrom, P. & Riekkel, C. (1996). *J. Appl. Phys.* **79**, 4471.
- Marcuse, D. (1991). *Theory of Dielectric Waveguides*. San Diego: Academic Press.
- Pfeiffer, F., David, C., Burghammer, M., Riekkel, C. & Salditt, T. (2002). *Science*, **297**, 230–234.
- Pfeiffer, F., Salditt, T., Hoghoi, P., Anderson, I. & Schell, N. (2000). *Phys. Rev. B*, **62**, 16939–16943.
- Scarmozzino, R. & Osgood, R. M. Jr (1991). *J. Opt. Soc. Am. B*, **8**, 724–731.
- Spiller, E. & Segmueller, A. (1974). *Appl. Phys. Lett.* **24**, 60.
- Tolansky, S. (1970). *Multiple Beam Interferometry of Surfaces and Films*. New York: Dover.
- Zwanenburg, M. J. (2001). PhD thesis, University of Amsterdam, The Netherlands.
- Zwanenburg, M. J., Bongaerts, J. H. H., Peters, J. F., Riese, D. O. & van der Veen, J. F. (2000). *Phys. Rev. Lett.* **85**, 5154–5157.
- Zwanenburg, M. J., Ficke, H. G., Neerings, H. & van der Veen, J. F. (2000). *Rev. Sci. Instrum.* **71**, 1723–1732.
- Zwanenburg, M. J., Peters, J. F., Bongaerts, J. H. H., de Vries, S. A., Abernathy, D. L. & van der Veen, J. F. (1999). *Phys. Rev. Lett.* **82**, 1696.